Research Article | Open Access

Microstructures

Liu et al. Microstructures 2026, 6, 2026094 DOI:10.20517/microstructures.2026.88

Perpendicular compensated ferrimagnetic tunnel junctions

Qi Liu[1,2,#], Pengfei Liu[3,4,#], Xiaowen Li[1], Shanquan Chen[1], Sixia Hu[2], Yao Wang[2], Zedong Xu[4], Songbai Hu[5], Mao Ye[6], Kaiyou Wang[3,7], Lang Chen[1,8,9]

Keywords:
Ferrimagnetic tunnel junctions, perpendicular magnetic anisotropy, non-volatile

Citation: Liu, Q.; Liu, P.; Li, X.; Chen, S.; Hu, S.; Wang, Y.; Xu, Z.; Hu, S.; Ye, M.; Wang, K.; Chen, L. Perpendicular compensated ferrimagnetic tunnel junctions. *Microstructures* **2026**, *6*, 2026094. https://dx.doi.org/10.20517/microstructures.2026.88

Received: 29 Apr 2026
First Decision: 26 May 2026
Revised: 10 Jun 2026
Accepted: 17 Jun 2026
Published: 9 Jul 2026

Academic Editor: Shiqing Deng
Copy Editor: Ping Zhang
Production Editor: Ping Zhang

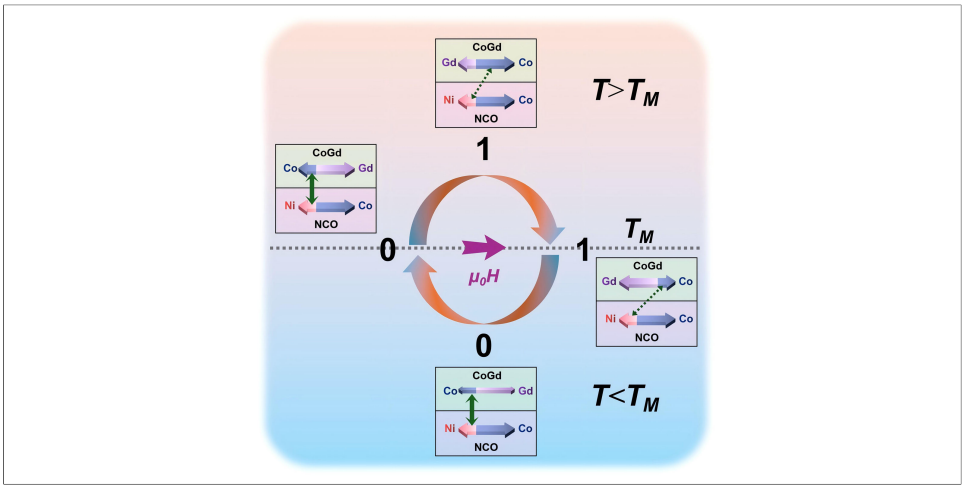

Abstract

Combining the advantages of ferromagnetic and antiferromagnetic tunnel junctions, ferrimagnetic tunnel junctions are highly desirable for spintronic applications. Here, we design and experimentally demonstrate a novel type of perpendicular compensated ferrimagnetic tunnel junction composed of the ferrimagnetic oxide $NiCo_2O_4$ and the compensated ferrimagnetic alloy $Co_{100-x}Gd_x$ separated by an $MgAl_2O_4$ insulating barrier. The tunneling magnetoresistance undergoes a sign transition from positive to negative (from +72% to -22%) as the temperature increases across the magnetization compensation point of $Co_{100-x}Gd_x$, which is attributed to the reversible magnetic dominance between the Co and Gd sublattices. Furthermore, we employ this ferrimagnetic tunnel

[1]Department of Physics, Southern University of Science and Technology, Shenzhen 518055, Guangdong, China.
[2]Core Research Facilities, Southern University of Science and Technology, Shenzhen 518055, Guangdong, China.
[3]State Key Laboratory of Semiconductor Physics and Chip Technologies, Institute of Semiconductors, Chinese Academy of Sciences, Beijing 100083, China.
[4]School of Electronics and Information Engineering, Tiangong University, Tianjin 300387, China.
[5]School of Physical Science, Great Bay University, Dongguan 523429, Guangdong, China.
[6]School of Physics and Materials Science, Guangzhou University, Guangzhou 510006, Guangdong, China.
[7]Center of Materials Science and Optoelectronics Engineering, University of Chinese Academy of Sciences, Beijing 100049, China.
[8]State Key Laboratory of Quantum Functional Materials, Southern University of Science and Technology, Shenzhen 518055, Guangdong, China.
[9]Guangdong Basic Research Center of Excellence for Quantum Science, Southern University of Science and Technology, Shenzhen 518055, Guangdong, China.
[#]These authors contributed equally to this work.

Correspondence to: Prof. Kaiyou Wang, State Key Laboratory of Semiconductor Physics and Chip Technologies, Institute of Semiconductors, Chinese Academy of Sciences, Beijing 100083, China; Center of Materials Science and Optoelectronics Engineering, University of Chinese Academy of Sciences, Beijing 100049, China. E-mail: kywang@semi.ac.cn; Prof. Lang Chen, Department of Physics,

Southern University of Science and Technology, Shenzhen 518055, Guangdong, China; State Key Laboratory of Quantum Functional Materials, Southern University of Science and Technology, Shenzhen 518055, Guangdong, China; Guangdong Basic Research Center of Excellence for Quantum Science, Southern University of Science and Technology, Shenzhen 518055, Guangdong, China. E-mail: chenlang@sustech.edu.cn

junction to realize temperature-dependent non-volatile multilevel states. Our findings on the perpendicular compensated ferrimagnetic tunnel junctions can provide an attractive avenue for developing ferrimagnet-based devices.

INTRODUCTION

Magnetic tunnel junctions (MTJs), which comprise two ferromagnetic (FM) layers separated by a thin insulating layer, serve as the core building blocks for magnetic random access memory (MRAM), spin logic devices, and brain-inspired computing systems[1-6]. Electron tunneling between two FM electrodes can be effectively controlled by switching the relative magnetization orientation between parallel (P) and antiparallel (AP) states. This effect is known as tunneling magnetoresistance (TMR) [Figure 1A][7-9]. However, the miniaturization of MTJ devices remains a critical challenge in spintronics, owing to stray fields generated within ferromagnetic layers [Figure 1B][10,11]. Moreover, the intrinsic slow spin dynamics of ferromagnets limit the operational speed of arithmetic devices[12]. Antiferromagnets (AFM) have become potential candidates for spintronic applications owing to their strong magnetic stability, zero stray fields and ultrafast dynamic responses [Figure 1B][13,14]. An antiferromagnetic tunnel junction (AFMTJ) consists of two AFM electrodes, and the P or AP alignment of their Néel vectors gives rise to the TMR effect [Figure 1A][7,8]. Antiferromagnets exhibit zero net magnetization, which greatly complicates the achievement of TMR in AFMTJs. To overcome these bottlenecks, ferrimagnets stand out as a promising candidate that combines the merits of ferromagnets and antiferromagnets simultaneously. Consisting of two sublattices with antiparallel but unequal magnetic moments, ferrimagnets produce tunable and detectable net magnetization and ultrafast spin dynamics. Owing to the limited net magnetization, ferrimagnets feature drastically suppressed stray fields relative to conventional ferromagnets, effectively mitigating edge-induced perturbations in scaled-down spintronic devices [Figure 1B][15-18]. As a result, perpendicular ferrimagnetic tunnel junctions possess great potential to boost the integration density of MTJ units and promote arithmetic frequency and operating speed.

Research studies on ferrimagnetic tunnel junctions have primarily focused on compensated ferrimagnets, composing Rare-earth (RE) and transition metals (RE-TM)[19-21]. Such materials exhibit a unique antiferromagnetic coupling between the non-equivalent magnetic moments of the RE and TM sublattices[22-24]. At a specific magnetization compensation temperature (T_M), the magnetic moments of the two sublattices become equivalent and opposite. Below and above T_M, the net magnetization is dominated by the RE and TM sublattices, respectively. By changing the temperature, the dominant sublattice responsible for the net magnetic moment can be switched[25,26]. Significant progress has been made in realizing TMR (~33% to 58%) and giant magnetoresistance (GMR) (~0.5%), particularly in CoFe/MgO/CoGd or CoFeB/MgO/CoFeB/CoTb tunnel junctions and CoFe/Cu/CoGd spin valves[27-29]. Despite these achievements, the presence of in-plane magnetic anisotropy and the ferromagnetic layer (CoFe) in the devices restrict further performance optimization. As a result, the development of perpendicular all-ferrimagnetic magnetic junctions remains highly desirable [Figure 1A].

In this work, we demonstrate a novel type of perpendicular compensated ferrimagnetic tunnel junctions, in which the compensated ferrimagnet $Co_{100-x}Gd_x$ and the ferrimagnetic metal oxide $NiCo_2O_4$ (NCO) are separated by an $MgAl_2O_4$ (MAO) insulating barrier. As a ferrimagnet, NCO exhibits robust perpendicular magnetic anisotropy (PMA) together with an extremely high spin polarization (theoretically up to 100%),

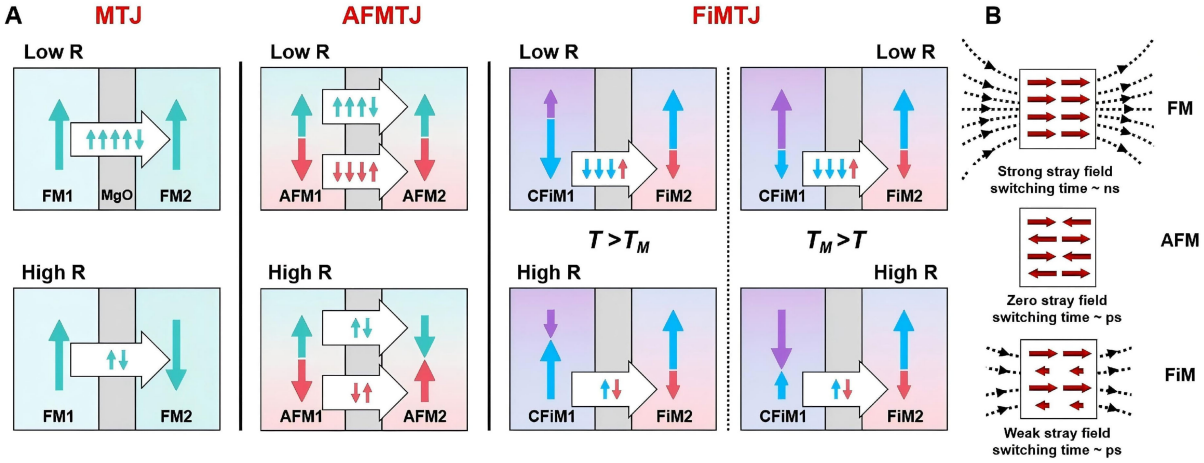

Figure 1. Schematics of different types of tunnel junctions. (A) Schematics of a conventional MTJ where two ferromagnetic (FM) electrodes are separated by a tunnel barrier. Conduction (indicated by block arrows) between the left and right FM electrodes for parallel and antiparallel magnetization (indicated by different colored arrows). Schematics of an antiferromagnetic tunnel junction (AFMTJ) with two AFM electrodes. Schematics of our ferrimagnetic tunnel junction (FiMTJ) with a compensated ferrimagnetic electrode (CFiM1) and another ferrimagnetic electrode (FiM2). Tunneling behavior at temperatures below and above T_M is illustrated; (B) Schematic comparison of magnetic configuration, stray fields, and spin dynamics of FM, AFM, and FiM. MTJ: Magnetic tunnel junction.

rendering it an ideal candidate for our ferrimagnetic tunnel junctions[30]. Intriguingly, we observe a sign transition of TMR (from +72% to -22%) as the temperature increases across the T_M point. This sign transition arises from the reversible switching of magnetic dominance between Co and Gd sublattices in the CoGd layer. Furthermore, the proposed ferrimagnetic devices can realize temperature-dependent non-volatile multilevel resistance states.

MATERIALS AND METHODS

Sample growth and device fabrication

The bilayers NCO (16 nm)/MAO (3 nm) were epitaxially deposited on (100)-oriented MAO substrates using a KrF excimer laser (λ = 248 nm) via a pulsed laser deposition (PLD) system. The ceramic targets NCO and MAO were prepared through solid-state reaction (supplied by ZhongNuo Advanced Material Technology Co., Ltd, Beijing). The deposition parameters were fixed at a substrate temperature of 350 °C, a laser energy density of 1.2 J/cm^2, and a pulse repetition rate of 7 Hz. The oxygen pressure during the deposition process was set as 200 mTorr for NCO and 50 mTorr for MAO, respectively. After the deposition, the multilayers were *in situ* annealed for 15 minutes under the oxygen pressure of 50 mTorr and then cooled down to room temperature under the oxygen pressure of 1,000 mTorr to suppress oxygen vacancy formation.

After deposition of the heterostructures, tunnel junction devices with varied dimensions were fabricated. All devices adopt uniform bottom electrode strips (NCO, 300 μm in width) and vertically interleaved top electrode strips (Co82Gd18/Pt, 100 μm in width) measuring around 100 μm in width. A 30 nm silicon oxide layer was deposited to electrically isolate the top and bottom electrodes. Effective junctions of different sizes are located at the intersection of the top and bottom electrodes. The detailed micro-nano fabrication process of the devices is illustrated in Supplementary Figure 1. Device patterning was performed using an Ultraviolet Maskless Lithography machine (TuoTuo Technology). The $Co_{82}Gd_{18}$ layers were deposited using a dual-target co-sputtering technique in a magnetron sputtering system with a base pressure lower than 5×10^{-8} Torr.

Magnetic measurements and magnetoresistance characterizations

Temperature-dependent magnetic characterizations of the films were conducted on a superconducting quantum interference device (SQUID), where in-plane magnetic fields were applied along the substrate [100] crystallographic direction and out-of-plane fields along the [001] orientation. Magnetoresistance measurements of ferrimagnetic tunnel junctions and anomalous Hall effect (AHE) measurements were implemented with a physical property measurement system (PPMS).

Electrical analysis and fitting

The Brinkman-Dynes-Rowell (BDR) model[31-35] used for analyzing tunneling conductance is described as

$$G(V)/G(0) = 1 - \left(\frac{A_0\Delta\phi}{16\sqrt{\bar{\phi}\bar{\phi}}}\right)\mathrm{eV} + \left(\frac{9}{128}\frac{A_0^2}{\bar{\phi}}\right)(\mathrm{eV})^2 \quad (1)$$

where the tunneling conductance at zero bias $G(0) = \left(3.16\times10^{10}\bar{\phi}^{-1/2}/d\right)\exp\left(-1.025d\bar{\phi}^{-1/2}\right)$, $A_0 = 4(2m)^{1/2}d/3\hbar$, d is the effective barrier thickness in Å, m_e is the effective mass, $\Delta\phi$ is the difference in the asymmetric interfacial barrier height in eV, and $\bar{\phi}$ is the average barrier height in eV. This expression is accurate to approximately 10% when the barrier thickness is greater than 10 Å and $\Delta\phi/\bar{\phi}$ is less than one.

The density functional theory calculations

Based on density of functional theory, all first-principles calculations were performed using the Vienna ab initio simulation package (VASP) code[36]. The exchange-correlation functional adopted the meta generalized gradient approximation (meta-GGA) of the strongly constrained and appropriately normed (SCAN) semilocal density functional[37]. SCAN function can satisfies all exact constraints applicable to existing density functionals, suggesting its superiority over most conventional gradient-corrected functionals. The heterostructure unit cell was calculated using the Γ-centered K-point mesh with a resolved value of 0.03 π/Å. The energy cut-off value is 450 eV, and the structures were completely relaxed until their atomic Hellmann-Feynman forces were less than 0.005 eV/Å. The convergence criterion of energy in the self-consistency process is 10^{-6} eV.

RESULTS AND DISCUSSION

First, the NCO (16 nm)/MAO (3 nm) bilayers with flat surface morphology were deposited on (100)-oriented MAO single-crystal substrates using a KrF excimer laser [Figure 2A]. Subsequently, $Co_{82}Gd_{18}$ (5 nm)/Pt (50 nm) bilayers were prepared by co-sputtering Co and Gd targets (see Experimental Section). The X-ray diffraction (XRD) patterns of NCO (16 nm), MAO (12 nm), and the NCO (16 nm)/MAO (3 nm) bilayers verify that all the crystallographic planes of these films are parallel to the (00*l*) planes of MAO [Figure 2B][38,39]. To evaluate the substrate-induced strain, reciprocal space mapping (RSM) was performed around the asymmetric (408) reflections [Figure 2C]. The almost identical in-plane scattering vectors Q_x indicate that the bilayer stack is epitaxially grown and fully strained[40]. High-resolution transmission electron microscopy (HRTEM) imaging of the cross section along the [100] zone axis was performed to further elucidate the interfacial features. The locally magnified atomic-resolution high-angle annular dark-field (HAADF) scanning transmission electron microscopy (STEM) image clearly reveals the stack of inverse spinel structures in NCO [Figure 2D][41]. The tetrahedral (T_d) sites are populated by the Co atoms, while the octahedral (O_h) sites are evenly occupied by the Ni and Co atoms[42,43]. In addition, the annular bright-field (ABF) STEM image and its corresponding energy-dispersive X-ray spectroscopy (EDS) indicate the high structural quality of our films and interfaces [Supplementary Figure 2].

We further investigate the spin-dependent transport properties of the ferrimagnetic layers: $Co_{82}Gd_{18}$ and NCO (see Experimental Section). Regarding the $Co_{82}Gd_{18}$ layer, the square-shaped AHE loops of the $Co_{82}Gd_{18}$/Pt confirm the presence of PMA [Figure 2E and F][44,45]. The temperature-induced reversal of

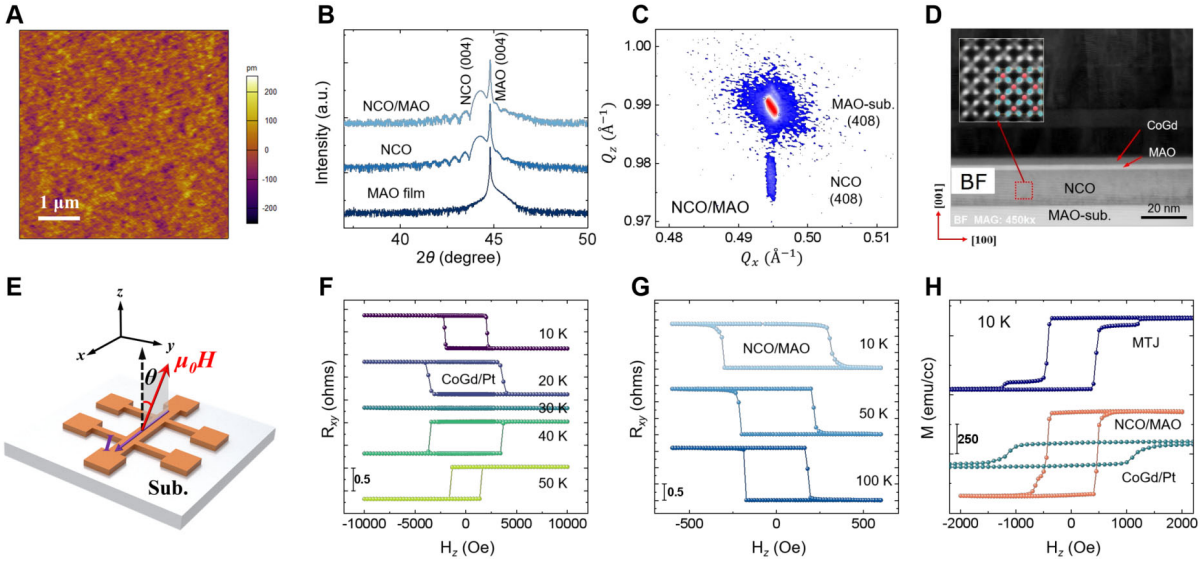

Figure 2. Structural characterization and spin-dependent performance of heterostructures. (A) Atomic force microscopy (AFM) image of the $NiCo_2O_4/MgAl_2O_4$ (NCO/MAO) bilayers with a root-mean-square (RMS) roughness of 0.05 nm. The length of the scale bar is 1 μm; (B) X-ray diffraction (XRD) patterns of MAO (12 nm), NCO (16 nm), and NCO (16 nm)/MAO (3 nm). The characteristic diffraction peaks at (004)-plane are indicated; (C) Reciprocal space mapping (RSM) of the (408) reflection of the NCO/MAO bilayers; (D) Annular bright-field (ABF) micrograph of the magnetic tunnel junction (MTJ) heterostructures along the [100] axis, with labels indicating different layers. The length of the scale bar is 20 nm. Inset: Atomic-resolution higher-magnification high-angle annular dark-field scanning transmission electron microscopy (HAADF-STEM) image of the region enclosed by the red dashed box, illustrating the unit cell scheme of the NCO crystal structure. Red and blue spheres represent T_d and O_h sites, respectively; (E) Schematic illustration of hall-bar device for anomalous Hall effect (AHE) measurements; (F) AHE loops of the $Co_{82}Gd_{18}$ (5 nm)/Pt (50 nm) bilayers at various temperatures; (G) AHE loops of the NCO (16 nm)/MAO (3 nm) bilayers at different temperatures; (H) Out-of-plane magnetic hysteresis loops of the NCO/MAO bilayers, $Co_{82}Gd_{18}$ /Pt bilayers, and MTJ heterostructures at 10 K. BF: Bright-field.

hysteresis loop chirality is attributed to the reversible magnetic dominance between the Co and Gd sublattices [Supplementary Figure 3A][46,47]. The sign of the anomalous Hall coefficient tracks the dominant sublattice magnetization, reversing when the net moment switches from Gd-dominated to Co-dominated. Meanwhile, the coercivity H_C increases steeply as the temperature approaches T_M from both sides [Supplementary Figure 3B-D], which arises from the enhanced Zeeman energy to switch the weakened magnetization[15]. Regarding the NCO layer, square AHE hysteresis loops indicate its intrinsic PMA behavior [Figure 2G], which is further validated by the temperature-dependent magnetization along the out-of-plane and in-plane directions [Supplementary Figure 4]. The magnetic moment of NCO primarily originates from the T_d-site Co atoms and the O_h-site Ni atoms, which exhibit antiparallel magnetic alignment[41]. The net magnetization and the PMA are dominated by the Co_{Td} atoms, while the electrical transport behavior is dominated by the Ni_{Oh} atoms[48]. Moreover, theoretical calculations verify that the majority spin state below the Fermi level dominantly originates from Co, while the minority spin state near the Fermi level dominantly originates from Ni[41]. This unique half-metallic band structure with a spin polarization of ~100% endows NCO with great potential for spintronic devices such as MTJs[30]. The out-of-plane magnetic hysteresis loop of the NCO/MAO/$Co_{82}Gd_{18}$ multilayers at 10 K is presented in Figure 2H. The distinct two-step switching corresponding to the coercivity of the NCO and CoGd layers respectively, guarantees the functional feasibility of the designed perpendicular ferrimagnetic tunnel junction[49,50].

Furthermore, we systematically investigate the TMR performance of the ferrimagnetic tunnel junction (junction size: *Dia*~2 μm, *A* ~3.1 μm^2) under out-of-plane magnetic fields (see Experimental Section). Notably, the TMR undergoes a clear sign transition from positive to negative as the temperature rises across the T_M of $Co_{82}Gd_{18}$ (~27 K) [Figure 3A]. In the TMR hysteresis loops, one switching occurs at a low magnetic

field (around 600 Oe), corresponding to the magnetization reversal of NCO. The second switching at a higher magnetic field is tunable from 2,500 Oe to 12,000 Oe and back to 1,600 Oe with increasing temperature from 10 K to 40 K, which is consistent with the changing coercivity of the $Co_{82}Gd_{18}$ layer. The TMR value is defined as $\mathrm{TMR} = \frac{R_{AP} - R_P}{R} \times 100\%$, where R_{AP} and R_P denote the resistances for the AP and P magnetization alignments of the two ferrimagnetic layers[51]. As illustrated in Figure 3B, a positive TMR ~26% is obtained below T_M, while a negative TMR of approximately -18% is observed above T_M (the reference curve is obtained from the junction with the highest signal-to-noise ratio. Error bars are defined as the signal deviation of the other two junctions within the same device array relative to this benchmark, and the error bars for all subsequent data share the same source). Our results are opposite to those of the in-plane ferrimagnetic TMR reported by Kaiser *et al.*[27], where the TMR sign reversal occurred from negative to positive[29]. This distinct behavior in our work originates from the Co_{Td} dominance in magnetization and Ni_{Oh} dominance in transport in the NCO layer, with the two coupled antiparallelly[48]. Moreover, at temperatures both below (15 K) and above (35 K) the T_M of $Co_{82}Gd_{18}$, the positive and negative TMR values decrease significantly as the magnetic field orientation approaches the in-plane direction [Figure 3C and D], verifying the perpendicular nature of our tunnel junction[39,52]. The angular-dependent TMR loops exhibit a pronounced increase in the coercivity for both NCO and $Co_{82}Gd_{18}$ [Supplementary Figure 5], which is attributed to the reduced out-of-plane component of the applied magnetic field[53,54]. It is consistent with the angular dependence of the AHE response for both NCO and $Co_{82}Gd_{18}$ films [Supplementary Figure 6].

In addition, the nonlinear *I-V* curves of the junction were measured across a temperature range of 100-200 K, demonstrating the high quality of the MAO barrier [Figure 3E][30]. The conductance ($G = dI/dV$) exhibits an approximately parabolic dependence on the bias voltage within the low-bias region, signifying a direct tunneling process[32,33], which can be fitted using the BDR model [Figure 3E, inset]. Notably, the TMR exhibits strong dependence on device dimension. The pronounced TMR improvement upon device downsizing primarily originates from suppressed parasitic leakage current [Figure 3F]. The optimized device yields maximum TMR values of approximately +72% at 2 K and -22% at 50 K [Supplementary Figure 7]. However, further device miniaturization leads to a degraded signal-to-noise ratio due to the inherent experimental limitations. According to the Jullière model, i.e., $\mathrm{TMR} = \frac{2P_1P_2}{1 - P_1P_2}$, assuming the spin polarization of NCO is -100%[30], the nominal spin polarization of our $Co_{82}Gd_{18}$ layer is estimated to be -26.5% below T_M (2 K) and +12.4% above T_M (50 K).

To elucidate the spin-dependent transport behavior in our perpendicular ferrimagnetic tunnel junctions, density functional theory (DFT) calculations of the NCO oxide and the CoGd alloy were performed (the structural models of CoGd and NCO are displayed in Figure 4A and 4B, respectively). For simplified modeling and reduced computational cost of DFT calculations, we adopted the $Co_{75}Gd_{25}$ model with an integer atomic stoichiometric ratio. In the calculated density of states (DOS), the majority of the occupied *f* states of Gd are located at ~4.5 eV below the Fermi energy level and contribute to the magnetic moment of Gd [Figure 4C]. For the CoGd alloy, the calculated average magnetic moments are ~+7.29 μ_B and ~-1.51 μ_B for each Gd and Co atom, respectively [Supplementary Table 1], suggesting the antiferromagnetic coupling between Gd and Co. The Hall conductance can be described as

$$\sigma_H^{xy} = \frac{-e^3\tau^2}{(2\pi)^3\hbar} \int d^3\boldsymbol{k}\, \mathrm{v}_x \left[(\mathbf{v} \times \boldsymbol{B}) \cdot \nabla_{\boldsymbol{k}}\right] \mathrm{v}_y \left(\frac{\partial f_0}{\partial \varepsilon}\right) \tag{2}$$

where τ is the momentum relaxation time, e is the electron charge, $\mathbf{v}$ is the velocity, $\mathbf{B} = (0, 0, B_z)$ is the magnetic field along the *z*-direction, ε is the energy, $\hbar$ is the Planck constant, and f_0 is the Fermi distribution function[55]. According to the key term $(\frac{\partial f_0}{\partial \varepsilon})$, the Hall conductance is dominated by the carriers at the Fermi level. The state occupation at the Fermi level in CoGd is dominated by the spin-down state of the *d* electrons in Co [Figure 4C], confirming that the spin-dependent transport is dominated by the Co sublattice.

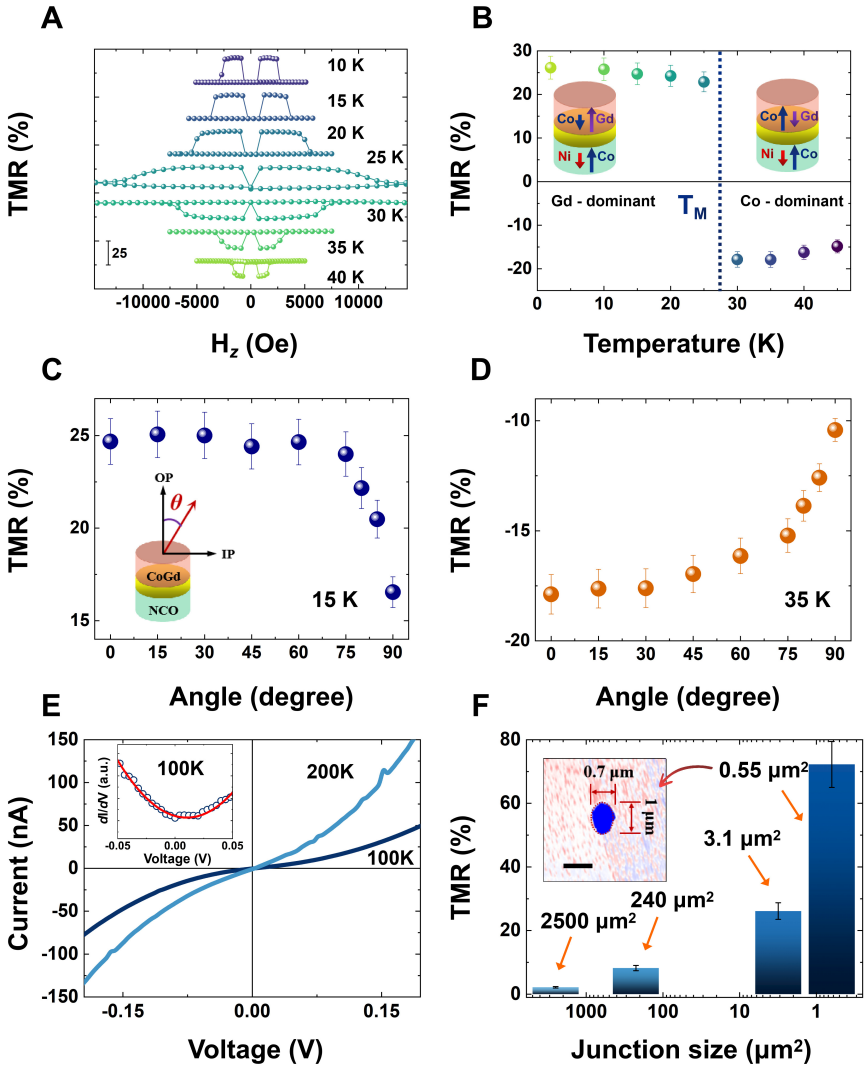

Figure 3. Tunneling characteristics of our perpendicular compensated ferrimagnetic tunnel junctions. (A) TMR loops obtained at various temperatures (using a reading bias of 1 mV); (B) Temperature dependence of the TMR values. Error bars are defined as the standard deviation (SD), the sample size is 3 and the error bars throughout this figure share the same source. Inset: A sketch illustrating the variation of antiferromagnetic coupling in $Co_{82}Gd_{18}$ when the temperature is below and above T_M; The dependence of the TMR value on the angle of the sweeping magnetic field at (C) 15 K and (D) 35 K. In these Figures, 0° and 90° correspond to the out-of-plane and in-plane magnetic field directions, respectively; (E) *I-V* curves (*Dia*-56 μm, *A* ~2,500 μm²) at various temperatures. Inset: Corresponding *dI/dV-V* curves in the low-bias region at 100 K, fitted using the BDR model; (F) Size-dependent TMR values of our ferrimagnetic tunnel junctions (Circles: *Dia* 56 μm, 17.5 μm, 2 μm, and ellipses: 1 μm × 0.7 μm). Inset: Surface morphology of the smallest device unit. The length of the scale bar is 1 μm. TMR: Tunneling magnetoresistance.

For the NCO, the magnetization is dominated by the *d* electrons of the Co_{Td} and Ni_{Oh} atoms, and the magnetic moments of the Co_{Td} and Ni_{Oh} atoms are estimated to be ~+2.41 μ_B and ~-0.55 μ_B, respectively [Supplementary Table 2]. As shown in Figure 4D, there are almost only spin-down occupied states at the Fermi energy level, confirming the half-metallic nature with a spin polarization of -100%[30,56]. Furthermore, according to the band structures near the Fermi energy level of Ni and Co [Figure 4E and F], the electrical transport of NCO is dominated by spin-down Ni_{Oh}. Combining the theoretical calculations, the magnetization and transport of the CoGd alloy are dominated by the Gd and Co sublattices, respectively. Besides, in NCO, the magnetization and transport are dominated by Co_{Td} and Ni_{Oh} atoms, respectively. Figure 4G presents the physical schematic of the sign-reversible TMR effect in our perpendicular

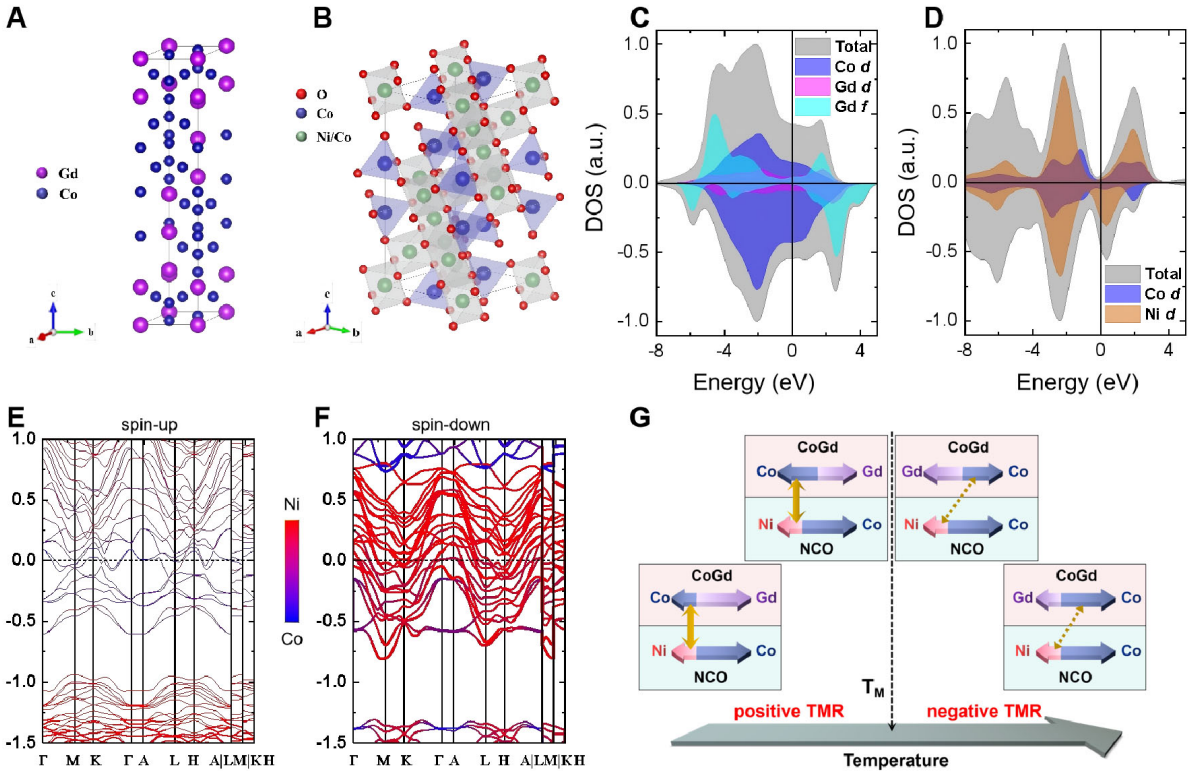

Figure 4. DFT calculations of CoGd and NCO. (A) Illustration of the $Co_{75}Gd_{25}$ structure for the DFT calculations; (B) Sketch of the inverse spinel structure of NCO for the DFT calculations; (C) Calculated total DOS, DOS of the Co *d* states, and DOS of the Gd *d* and *f* states in CoGd; (D) Calculated total DOS and DOS of the Co and Ni *d* states in NCO; The calculated band structures of (E) spin-up and (F) spin-down states of Co and Ni near the Fermi level in NCO; (G) Illustration of the temperature-dependent tunneling behavior when the temperature is below, near, and above T_M. MAO: $MgAl_2O_4$; NCO: $NiCo_2O_4$; DFT: density functional theory; TMR: tunneling magnetoresistance; DOS: density of states.

compensated ferrimagnetic tunnel junctions. At temperatures below T_M, the applied magnetic field aligns the Co_{Td} moments in NCO parallel to the dominating Gd moments in CoGd. Tunneling occurs between the Co moments in CoGd and the Ni_{Oh} moments in NCO, which are aligned in parallel (oriented opposite to the magnetic field), giving rise to a positive TMR. At temperatures above T_M, the magnetic field aligns the Co_{Td} moments in NCO parallel to the dominating Co moments in CoGd. In this case, the Ni_{Oh} moments in NCO are aligned antiparallel to the Co moments in CoGd, thereby producing a negative TMR.

Benefiting from the temperature-dependent behavior inherent in our ferrimagnetic tunnel junction, the tunneling magnetoresistance states exhibit tunability to temperature modulation, enabling the realization of temperature-dependent non-volatile multilevel resistance states. The tunneling resistance states "0" and "1" at 20 K can be tuned through a heating-up and cooling-down process between 20 K and 40 K, assisted by a fixed magnetic field of 0.3 T [Figure 5A]. During the thermal cycling, the magnetic dominance between Co and Gd sublattices is switched, and the magnetic field fixes the net moment direction when the temperature crosses T_M. Once the resistance state is written, it remains non-volatile as the temperature returns to 20 K. Conversely, the resistance state can be reset to the "0" level through a cooling and warming cycle between 20 K and 10 K [Figure 5B]. The $Co_{82}Gd_{18}$ layer undergoes a reduction in the coercivity, and the fixed magnetic field becomes sufficient to accomplish the magnetization reversal[45]. Based on the above mechanisms, temperature-dependent non-volatile multilevel resistance states operating across T_M have been demonstrated. With the assistance of a fixed magnetic field of 0.3 T, the tunneling resistance states can be repeatedly rewritten between "0" or "1" through temperature modulation, delivering reliable non-volatile

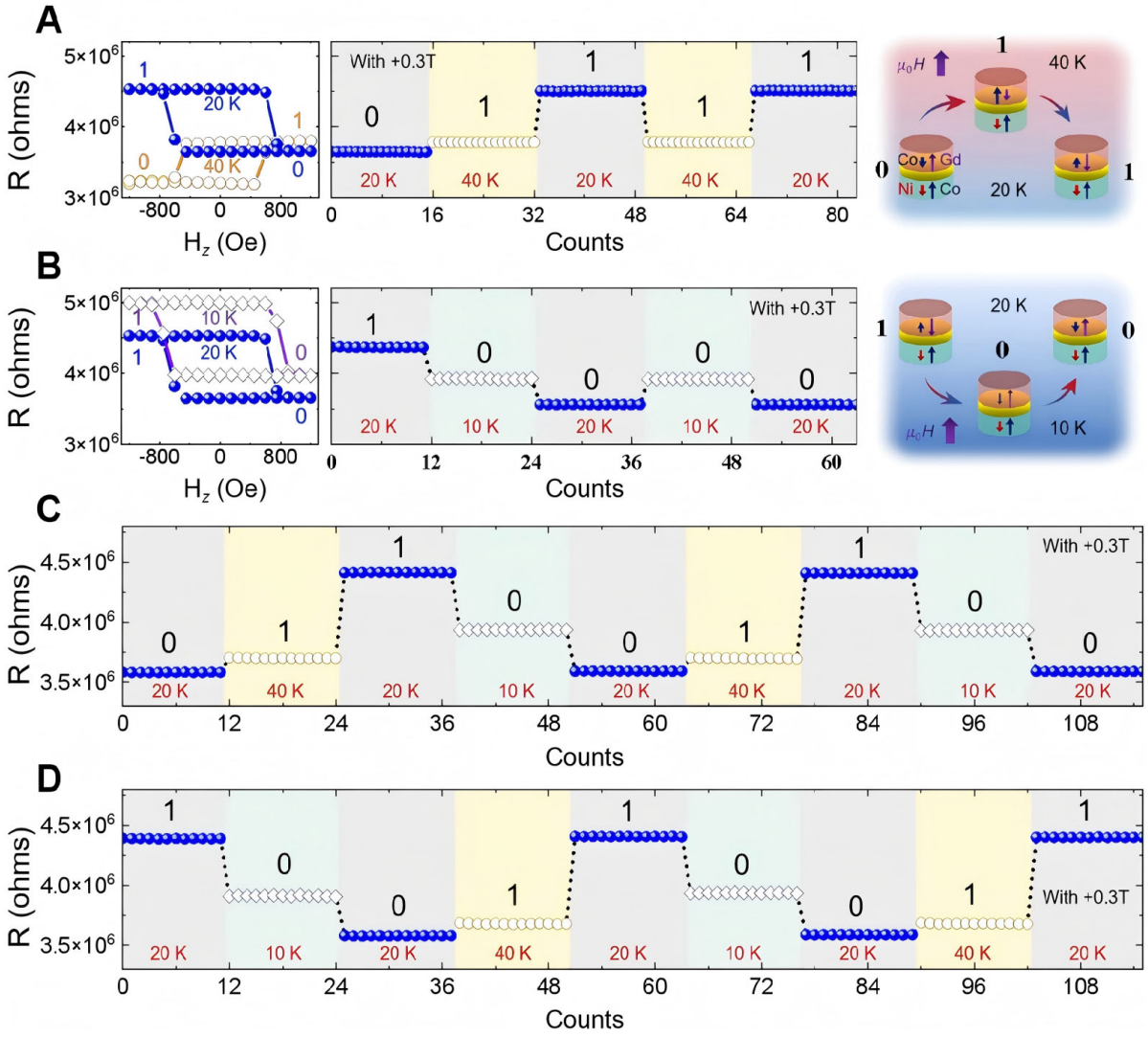

Figure 5. Temperature-dependent non-volatile multilevel states. TMR loops within a small magnetic field range, temperature-dependent non-volatile multilevel states assisted by a fixed magnetic field (+0.3 T), and mechanism illustration within (A) 20~40 K and (B) 10~20 K. "0" and "1" correspond to the low and high resistance states at the corresponding temperatures; Temperature-dependent non-volatile multilevel states within 10~40 K starting from different initial states: (C) "0" and (D) "1" assisted by a fixed magnetic field (+0.3 T). TMR: Tunneling magnetoresistance.

state manipulation [Figure 5C and D]. However, when the fixed magnetic field falls outside the appropriate range, volatile resistance variations are observed by varying the temperature [Supplementary Figures 8 and 9].

CONCLUSION

In summary, we have successfully demonstrated the perpendicular compensated ferrimagnetic tunnel junction based on the NCO/MAO/$Co_{82}Gd_{18}$ heterostructures, which exhibits reversible TMR sign switching (from +72% to -22%) as the temperature increases across the magnetization compensation point of $Co_{82}Gd_{18}$. The TMR sign switching is attributed to the thermally reversible magnetic compensation in $Co_{82}Gd_{18}$. Furthermore, we have applied this device to demonstrate temperature-dependent non-volatile multilevel resistance states. Unlike conventional MTJs, our ferrimagnetic tunnel junctions feature stray-field-free operation, temperature-tunable TMR polarity, and non-volatile multilevel resistance states. Utilizing our perpendicular compensated ferrimagnetic tunnel junctions, higher unit density, faster operating speed, and

enhanced device controllability are foreseeable for future spintronic applications. Our findings offer a promising route for the design and development of ferrimagnet-based spintronic devices.

DECLARATIONS

Authors' contributions

The conception and design of the work: Liu, Q.; Liu, P.; Wang, K.; Chen, L.
The acquisition and analysis of data: Liu, Q.; Liu, P.; Hu, S.; Wang, Y.
The theoretical calculations: Li, X.
The interpretation of data: Liu, Q.; Liu, P.; Chen, S.; Xu, Z.; Hu, S.; Ye, M.
The writing and revising: Liu, Q.; Liu, P.; Li, X.; Wang, K.; Chen, L.
The supervision: Wang, K.; Chen, L.

Availability of data and materials

The raw data supporting the findings of this study are available within this Article and its Supplementary Materials. Further data is available from the corresponding authors upon reasonable request.

AI and AI-assisted tools statement

Not applicable.

Financial support and sponsorship

This work was supported by the National Key R&D Program of China (Grant No. 2022YFA1402903), National Key Research and Development Program of China (Grant No. 2022YFA1405100), National Natural Science Foundation of China (Grant Nos. 12574096, 12504076, 12241405, 12304154 and 52025025), Postdoctoral Fellowship Program of CPSF (Grant No. GZC20252187), the Shenzhen Fundamental Research Program (Grant No. JCYJ20250604144519025) and SUSTech Core Research Facilities.

Conflicts of interest

All authors declared that there are no conflicts of interest.

Ethical approval and consent to participate

Not applicable.

Consent for publication

Not applicable.

Consent for publication

Not applicable.

Supplementary Materials

Supplementary Materials

REFERENCES

1. Yuasa, S.; Nagahama, T.; Fukushima, A.; Suzuki, Y.; Ando, K. Giant room-temperature magnetoresistance in single-crystal Fe/MgO/Fe magnetic tunnel junctions. *Nat. Mater.* **2004**, *3*, 868-71. DOI PubMed
2. Yang, H.; Valenzuela, S. O.; Chshiev, M.; et al. Two-dimensional materials prospects for non-volatile spintronic memories. *Nature* **2022**, *606*, 663-73. DOI
3. Cai, K.; Yang, M.; Ju, H.; et al. Electric field control of deterministic current-induced magnetization switching in a hybrid ferromagnetic/ferroelectric structure. *Nat. Mater.* **2017**, *16*, 712-6. DOI
4. Cao, Y.; Sheng, Y.; Edmonds, K. W.; Ji, Y.; Zheng, H.; Wang, K. Deterministic magnetization switching using lateral spin-orbit torque. *Adv. Mater.* **2020**, *32*, e1907929. DOI

5. Cao, Y.; Rushforth, A.; Sheng, Y.; Zheng, H.; Wang, K. Tuning a binary ferromagnet into a multistate synapse with spin-orbit-torque-induced plasticity. *Adv. Funct. Mater.* **2019**, *29*, 1808104. DOI
6. Xue, F.; Zhang, C.; Ma, Y.; et al. Integrated memory devices based on 2D materials. *Adv. Mater.* **2022**, *34*, e2201880. DOI
7. Gurung, G.; Elekhtiar, M.; Luo, Q. Q.; Shao, D. F.; Tsymbal, E. Y. Nearly perfect spin polarization of noncollinear antiferromagnets. *Nat. Commun.* **2024**, *15*, 10242. DOI PubMed PMC
8. Shao, D.; Tsymbal, E. Y. Antiferromagnetic tunnel junctions for spintronics. *npj. Spintronics.* **2024**, *2*, 14. DOI
9. Echtenkamp, W.; Dixit, B.; Yang, Y.; et al. Prospects of electric field control in perpendicular magnetic tunnel junctions and emerging 2D spintronics for ultralow energy memory and logic devices. *Adv. Funct. Mater.* **2026**, *36*, 2505426. DOI
10. Freeman, M. R.; Choi, B. C. Advances in magnetic microscopy. *Science* **2001**, *294*, 1484-8. DOI PubMed
11. Zhou, S.; Wang, Y.; Liu, Y. Modelling of magnetic stray fields in multilayer magnetic films with in-plane or perpendicular anisotropy. *Magnetochemistry* **2022**, *8*, 159. DOI
12. De Ranieri, E.; Roy, P. E.; Fang, D.; et al. Piezoelectric control of the mobility of a domain wall driven by adiabatic and non-adiabatic torques. *Nat. Mater.* **2013**, *12*, 808-14. DOI
13. Kimel, A. V.; Ivanov, B. A.; Pisarev, R. V.; Usachev, P. A.; Kirilyuk, A.; Rasing, T. Inertia-driven spin switching in antiferromagnets. *Nat. Phys.* **2009**, *5*, 727-31. DOI
14. Han, J.; Cheng, R.; Liu, L.; Ohno, H.; Fukami, S. Coherent antiferromagnetic spintronics. *Nat. Mater.* **2023**, *22*, 684-95. DOI
15. Kim, K. J.; Kim, S. K.; Hirata, Y.; et al. Fast domain wall motion in the vicinity of the angular momentum compensation temperature of ferrimagnets. *Nat. Mater.* **2017**, *16*, 1187-92. DOI
16. Kim, C.; Lee, S.; Kim, H. G.; et al. Distinct handedness of spin wave across the compensation temperatures of ferrimagnets. *Nat. Mater.* **2020**, *19*, 980-5. DOI
17. Din, A.; Amin, O. J.; Wadley, P.; Edmonds, K. W. Antiferromagnetic spintronics and beyond. *npj. Spintronics.* **2024**, *2*, 29. DOI
18. Kim, S. K.; Beach, G. S. D.; Lee, K. J.; Ono, T.; Rasing, T.; Yang, H. Ferrimagnetic spintronics. *Nat. Mater.* **2022**, *21*, 24-34. DOI PubMed
19. Ishibashi, M.; Yakushiji, K.; Kawaguchi, M.; Tsukamoto, A.; Nakatsuji, S.; Hayashi, M. Ferrimagnetic compensation and its thickness dependence in TbFeCo alloy thin films. *Appl. Phys. Lett.* **2022**, *120*, 022405. DOI
20. Finley, J.; Liu, L. Spintronics with compensated ferrimagnets. *Appl. Phys. Lett.* **2020**, *116*, 110501. DOI
21. Kiphart, D.; Chaves O'Flynn, G. D.; Stobiecki, F.; Frąckowiak, Ł.; Matczak, M.; Kuświk, P. Tailoring ferrimagnetic properties using proximity effects in Co/Tb-Co bilayers. *Adv. Mater. Interfaces.* **2025**, *12*, e00330. DOI
22. Ueda, K.; Mann, M.; de Brouwer, P. W. P.; Bono, D.; Beach, G. S. D. Temperature dependence of spin-orbit torques across the magnetic compensation point in a ferrimagnetic TbCo alloy film. *Phys. Rev. B.* **2017**, *96*, 064410. DOI
23. Wang, J.; Li, B.; An, Y.; Song, G.; Zhang, S. Interplay between magnetization compensation temperature and thickness in ferrimagnetic CoGd alloy films. *Appl. Phys. Lett.* **2025**, *126*, 072401. DOI
24. Xu, T.; Cheng, Y.; Dong, Y.; et al. Evolution of compensated magnetism and spin-torque switching in ferrimagnetic $Fe_{1-x}Tb_x$. *Phys. Rev. Appl.* **2023**, 19. DOI
25. Mishra, R.; Yu, J.; Qiu, X.; Motapothula, M.; Venkatesan, T.; Yang, H. Anomalous current-induced spin torques in ferrimagnets near compensation. *Phys. Rev. Lett.* **2017**, *118*, 167201. DOI PubMed
26. Li, Y.; Huang, S.; Zhu, W.; et al. Spin-canting mediated anomalous nernst effect in ferrimagnetic CoTb films. *Chinese. Phys. Lett.* **2026**, *43*, 020708. DOI
27. Kaiser, C.; Panchula, A. F.; Parkin, S. S. Finite tunneling spin polarization at the compensation point of rare-earth-metal-transition-metal alloys. *Phys. Rev. Lett.* **2005**, *95*, 047202. DOI PubMed
28. Zhu, W.; Tang, M.; Pan, C.; et al. Sign-tunable magnetic tunnel junctions engineered via ferrimagnets for efficient all-electrical and thermal switching. *Adv. Funct. Mater.* **2026**, *36*, 2505415. DOI
29. Jiang, X.; Gao, L.; Sun, J. Z.; Parkin, S. S. Temperature dependence of current-induced magnetization switching in spin valves with a ferrimagnetic CoGd free layer. *Phys. Rev. Lett.* **2006**, *97*, 217202. DOI
30. Shen, Y.; Kan, D.; Lin, I.; Chu, M.; Suzuki, I.; Shimakawa, Y. Perpendicular magnetic tunnel junctions based on half-metallic $NiCo_2O_4$. *Appl. Phys. Lett.* **2020**, *117*, 042408. DOI
31. Brinkman, W. F.; Dynes, R. C.; Rowell, J. M. Tunneling conductance of asymmetrical barriers. *J. Appl. Phys.* **1970**, *41*, 1915-21. DOI
32. Miller, C. W.; Li, Z. P.; Schuller, I. K.; Dave, R. W.; Slaughter, J. M.; Akerman, J. Dynamic spin-polarized resonant tunneling in magnetic tunnel junctions. *Phys. Rev. Lett.* **2007**, *99*, 047206. DOI PubMed
33. Santos, T. S.; Lee, J. S.; Migdal, P.; Lekshmi, I. C.; Satpati, B.; Moodera, J. S. Room-temperature tunnel magnetoresistance and spin-polarized tunneling through an organic semiconductor barrier. *Phys. Rev. Lett.* **2007**, *98*, 016601. DOI PubMed
34. Kaiser, B.; Ramberger, J.; Norum, M.; Nandakumaran, N.; Dewey, J.; Leighton, C. Optimizing nonlocal spin valves via wide-range interfacial-resistance tuning: Toward spin-accumulation sensors. *Phys. Rev. Appl.* **2024**, 22. DOI

35. Oliver, B.; Nowak, J. Temperature and bias dependence of dynamic conductance-low resistive magnetic tunnel junctions. *J. Appl. Phys.* **2004**, *95*, 546-50. DOI
36. Kresse, G.; Furthmüller, J. Efficient iterative schemes for ab initio total-energy calculations using a plane-wave basis set. *Phys. Rev. B.* **1996**, *54*, 11169-86. DOI
37. Sun, J.; Ruzsinszky, A.; Perdew, J. P. Strongly constrained and appropriately normed semilocal density functional. *Phys. Rev. Lett.* **2015**, *115*, 036402. DOI PubMed
38. Vasiukov, D. M.; Kareev, M.; Wen, F.; et al. Epitaxial stabilization of thin films of the frustrated Ge-based spinels. *Phys. Rev. Mater.* **2021**, *5*, 064419. DOI
39. Liu, Q.; Li, X.; Zhu, Y.; et al. Oxygen controlled perpendicular magnetic anisotropy in $LaCoO_{3-\delta}/La_{0.7}Sr_{0.3}MnO_3/LaCoO_{3-\delta}$ heterostructures. *Appl. Phys. Lett.* **2022**, *120*, 242902. DOI
40. Liu, Q.; Liu, P.; Li, X.; et al. Perpendicular manganite magnetic tunnel junctions induced by interfacial coupling. *ACS. Appl. Mater. Interfaces.* **2022**, *14*, 13883-90. DOI
41. Chen, X.; Zhang, X.; Han, M. G.; et al. Magnetotransport anomaly in room-temperature ferrimagnetic $NiCo_2O_4$ thin films. *Adv. Mater.* **2019**, *31*, e1805260. DOI
42. Kan, D.; Mizumaki, M.; Kitamura, M.; et al. Spin and orbital magnetic moments in perpendicularly magnetized $Ni_{1-x}Co_{2+y}O_{4-z}$ epitaxial thin films: effects of site-dependent cation valence states. *Phys. Rev. B.* **2020**, *101*, 224434. DOI
43. Bitla, Y.; Chin, Y. Y.; Lin, J. C.; et al. Origin of metallic behavior in $NiCo_2O_4$ ferrimagnet. *Sci. Rep.* **2015**, *5*, 15201. DOI PubMed PMC
44. Siddiqui, S. A.; Han, J.; Finley, J. T.; Ross, C. A.; Liu, L. Current-induced domain wall motion in a compensated ferrimagnet. *Phys. Rev. Lett.* **2018**, *121*, 057701. DOI
45. Meo, A.; Sha, C.; Darwin, E.; et al. Spin-wave eigenmodes in nanoscale magnetic tunnel junctions with perpendicular magnetic anisotropy. *Phys. Rev. Appl.* **2025**, *23*, 034086. DOI
46. Chen, D.; Xu, Y.; Tong, S.; et al. Noncollinear spin state and unusual magnetoresistance in ferrimagnet Co-Gd. *Phys. Rev. Materials.* **2022**, *6*, 014402. DOI
47. Park, J.; Hirata, Y.; Kang, J.; et al. Unconventional magnetoresistance induced by sperimagnetism in GdFeCo. *Phys. Rev. B.* **2021**, *103*, 014421. DOI
48. Shen, Y.; Kan, D.; Tan, Z.; Wakabayashi, Y.; Shimakawa, Y. Tuning of ferrimagnetism and perpendicular magnetic anisotropy in $NiCo_2O_4$ epitaxial films by the cation distribution. *Phys. Rev. B.* **2020**, *101*, 094412. DOI
49. Rivas-Murias, B.; Lucas, I.; Jiménez-Cavero, P.; Magén, C.; Morellón, L.; Rivadulla, F. Independent control of the magnetization in ferromagnetic $La_{2/3}Sr_{1/3}MnO_3/SrTiO_3/LaCoO_3$ heterostructures achieved by epitaxial lattice mismatch. *Nano. Lett.* **2016**, *16*, 1736-40. DOI PubMed
50. Wu, H.; Chen, A.; Zhang, P.; et al. Magnetic memory driven by topological insulators. *Nat. Commun.* **2021**, *12*, 6251. DOI PubMed PMC
51. Currivan-Incorvia, J. A.; Siddiqui, S.; Dutta, S.; et al. Logic circuit prototypes for three-terminal magnetic tunnel junctions with mobile domain walls. *Nat. Commun.* **2016**, *7*, 10275. DOI PubMed PMC
52. Bartolomé, J.; Arauzo, A.; Kazak, N. V.; et al. Uniaxial magnetic anisotropy in $Co_{2.25}Fe_{0.75}O_2BO_3$ compared to $Co_3O_2BO_3$ and Fe_3O_2BO ludwigites. *Phys. Rev. B.* **2011**, *83*, 144426. DOI
53. Kou, X.; Pan, L.; Wang, J.; et al. Metal-to-insulator switching in quantum anomalous Hall states. *Nat. Commun.* **2015**, *6*, 8474. DOI PubMed PMC
54. Liu, L.; Qin, Q.; Lin, W.; et al. Current-induced magnetization switching in all-oxide heterostructures. *Nat. Nanotechnol.* **2019**, *14*, 939-44. DOI
55. Hurd, C. M. The hall effect in metals and alloys. Springer Science & Business Media, 2012. DOI
56. Chang, T. C.; Lu, Y. T.; Lee, C. H.; et al. The effect of degrees of inversion on the electronic structure of spinel NiCo2O4: a density functional theory study. *ACS. Omega.* **2021**, *6*, 9692-9. DOI